# ROUTE, INTERPRET, REPEAT: BLURRING THE LINE BETWEEN POST HOC EXPLAINABILITY AND INTERPRETABLE MODELS

**Anonymous authors**
Paper under double-blind review

## ABSTRACT

The current approach to ML model design is either to choose a flexible Blackbox model and explain it post hoc or to start with an interpretable model. Blackbox models are flexible but difficult to explain, whereas interpretable models are designed to be explainable. However, developing interpretable models necessitates extensive ML knowledge, and the resulting models tend to be less flexible, offering potentially subpar performance compared to their Blackbox equivalents. This paper aims to blur the distinction between a post hoc explanation of a BlackBox and constructing interpretable models. We propose beginning with a flexible BlackBox model and gradually *carving out* a mixture of interpretable models and a *residual network*. Our design identifies a subset of samples and *routes* them through the interpretable models. The remaining samples are routed through a flexible residual network. We adopt First Order Logic (FOL) as the interpretable model's backbone, which provides basic reasoning on concepts retrieved from the BlackBox model. On the residual network, we repeat the method until the proportion of data explained by the residual network falls below a desired threshold. Our approach offers several advantages. First, the mixture of interpretable and flexible residual networks results in almost no compromise in performance. Second, the route, interpret, and repeat approach yields a highly flexible interpretable model. Our extensive experiment demonstrates the performance of the model on various datasets. We show that by editing the FOL model, we can fix the shortcut learned by the original BlackBox model. Finally, our method provides a framework for a hybrid symbolic-connectionist network that is simple to train and adaptable to many applications.

## 1 INTRODUCTION

Model explainability is essential in high-stakes applications of AI, such as healthcare. While BlackBox models (*e.g.,* Deep Learning) offer flexibility and modular design, post hoc explanation is prone to confirmation bias Wan et al. (2022), lack of fidelity to the original model Adebayo et al. (2018), and insufficient mechanistic explanation of the decision-making process Rudin (2019). Interpretable-by-design models do not suffer from those issues but tend to be less flexible than Blackbox models and demand substantial expertise to design and fine-tune. Using post hoc explanation or adopting an interpretable model is a mutually exclusive decision to be made at the initial phase of AI model design. This paper aims to blur the line on that dichotomous model design.

The literature on post hoc explainable AI is extensive. The methods such as model attribution (*e.g.,* Saliency Map Simonyan et al. (2013); Selvaraju et al. (2017)), counterfactual approach Abid et al. (2021); Singla et al. (2019), and distillation methods Alharbi et al. (2021); Cheng et al. (2020) are examples of post hoc explainability approaches. Those methods either identify important features of input that contribute the most to the network's output Shrikumar et al. (2016), generate perturbation to the input that flips the network's output Samek et al. (2016), Montavon et al. (2018), or estimate simpler functions that locally approximate the network output. The advantage of the post hoc explainability methods is that they do not compromise the flexibility and performance of the BlackBox. However, the post hoc explainability method suffers from several undesirable significant drawbacks, such as a lack of fidelity and mechanistic explanation of the network output Rudin

(2019). Without a mechanistic explanation, recourse to a model's undesirable behavior is unclear. Interpretable models are alternative designs to the BlackBox model that do not suffer from many of those drawbacks.

Interpretable models also have a long history in statistics and machine learning Letham et al. (2015); Breiman et al. (1984). Several families of interpretable models exist, such as the rule-based approach and generalized additive models Hastie & Tibshirani (1987). Many methods focus on tabular or categorical data and less on high-dimensional structured data such as images. Interpretable models for structured data rely mostly on projecting to a lower dimensional *concept* or *symbolic* space that is understandable for humans Koh et al. (2020). Aside from a few exceptions Ciravegna et al. (2021); Barbiero et al. (2022), the current State-Of-The-Art (SOTA) design does not model the interaction between concepts and symbols, hence offering limited reasoning capabilities and less robustness. Furthermore, current designs are not as flexible as the Blackbox model, which may compromise the performance of such models.

We aim to achieve the best of both worlds: the flexibility of the BlackBox and the mechanistic explainability of the interpretable models. The general idea is that a single interpretable model may not be sufficiently powerful to explain all samples, and several interpretable models might be hidden inside the Blackbox model. We construct a hybrid neuro-symbolic model by progressively *carving out* a mixture of interpretable model and a *residual network*. Our design identifies a subset of samples and *routes* them through the interpretable models. The remaining samples are routed through a flexible residual network. We adopt First Order Logic (FOL) as the interpretable model's backbone, which provides basic reasoning on concepts retrieved from the BlackBox model. FOL is a logical function that accepts predicates (concept presence/absent) as input and returns a True/False output being a logical expression of the predicates. The logical expression, which is a set of AND, OR, Negative, and parenthesis, can be written in the so-called Disjunctive Normal Form (DNF). DNF is a FOL logical formula composed of a disjunction (OR) of conjunctions (AND), known as the "sum of products." On the residual network, we repeat the method until the proportion of data explained by the residual network falls below a desired threshold. The experimental results across various computer vision and medical imaging datasets reveal that our method accounts for the diversity of the explanation space and has minimal impact on the Blackbox's performance. Additionally, we apply our method's explanations to detect shortcuts in computer vision and successfully eliminate the bias from the Blackbox's representation.

## 2 Related work

**Post hoc explanations** Simonyan et al. (2013); Selvaraju et al. (2017); Smilkov et al. (2017) discuss the post hoc based explanation method using saliency maps to explain a convolution neural network. This method aims to highlight the pixels in the input images that contributed to the network's prediction. Adebayo et al. (2018); Kindermans et al. (2019) demonstrates that the saliency maps highlight the correct regions in the image even though the backbone's representation was arbitrarily perturbed. Additionally, in LIME Ribeiro et al. (2016), given a superpixel, a surrogate linear function attempts to learn the prediction of the Blackbox surrounding that superpixel. SHAP Lundberg & Lee (2017) utilizes a prominent game-theoretic strategy called SHAPLY values to estimate the Blackbox's prediction by considering all the permutations of adding and removing a specific feature to determine its importance in the final prediction. Having the explainations in terms of pixel intensities, they do not correspond to the high-level interpretable attributes (*concept*), understood by humans. In this paper, we aim to provide the post hoc explanation of the Blackbox in terms of the interpretable concepts, rather than the pixel intensities.

**Interpretable models** In this class, the researchers try to design inherently interpretable models to eliminate the requirement for post hoc explanations. In the literature, we find interpretable models in Generalized Additive Models (GAM) Hastie & Tibshirani (1987), or on logic formulas, as in Decision Trees Breiman et al. (1984) or Bayesian Rule Lists (BRL) Letham et al. (2015). However, most of these methods work well in categorical datasets rather than continuous data such as images. Additionally, a "case-based reasoning" technique was introduced in Chen et al. (2019); Nauta et al. (2021). Here, the authors first dissect an image in Prototypical parts and then classifies by combining evidence from the pre-defined prototypes. This method is highly sensitive to the choice of prototypes

and the distance metric used to compare with the prototype. So instead of using any prototypes, our proposed method uses human understandable concepts to build the mixture of interpretable models.

**Concept-based interpretable models** Recently, Concept bottleneck models (CBM) Koh et al. (2020) leverage the weak annotations of visual attributes as high-level human-comprehensible concepts Kim et al. (2017) in a fine-grained image classification dataset to predict the concepts from input images. Subsequently, the downstream classifier predicts the class labels from the discovered concepts. However, they do not explain how the final classifier composes those concepts for prediction. LENs Ciravegna et al. (2021) utilizes a constratint based approch from Ciravegna et al. (2020a), Ciravegna et al. (2020b) to address this gap by providing explanations in terms of first-order logic (FOL) using the concepts. However, a strong pruning strategy and L1 regularization hinders the learning capability of LENs. E-Lens Barbiero et al. (2022) solves this problem by introducing an attention driven entropy layer which focuses on the relevant concept for downstream classification. Later, Yuksekgonul et al. (2022) introduces the Post hoc-concept-based model (PCBM) to learn the concepts from the backbone of a trained Blackbox and utilize an interpretable classifier to learn the class labels from the concepts. In addition, they propose the Hybrid-Post hoc-concept-based model (PCBM-h) to replicate the performance of the original Blackbox by fitting the unexplained portion of the Blackbox. However, all these methods either employ a single interpretable by design model or a single surrogate model to explain a Blackbox, failing to apprehend different form of explanations for different samples. This paper proposes that a single interpretable model may not be sufficient to capture the diversity of explanations for all samples used by the Blackbox. We address this issue by introducing a mixture of interpretable models that utilizes the Blackbox's flexibility and offer a local explanation.

## 3 METHOD

**Notation** Assume we have a dataset $\{\mathcal{X}, \mathcal{Y}, \mathcal{C}\}$, where $\mathcal{X}$, $\mathcal{Y}$, and $\mathcal{C}$ are the input images, class labels, and human interpretable attributes, respectively. $f^0 : \mathcal{X} \rightarrow \mathcal{Y}$, is a pre-trained deep neural network (our initial Blackbox model), trained only with supervision from the labels $\mathcal{Y}$. We assume that $f^0$ is a composition $h^0 \circ \Phi$, where $\Phi : \mathcal{X} \rightarrow \mathbb{R}^l$ is the image embeddings and $h^0 : \mathbb{R}^l \rightarrow \mathcal{Y}$ is a transformation from the embeddings, $\Phi$, to the class labels. We denote the learnable function $t : \mathbb{R}^l \rightarrow \mathcal{C}$, projecting the image embeddings to the concept space. The concept space is the space spanned by the attributes $\mathcal{C}$. Per this definition, function $t$ outputs a scalar value representing a concept for each input image.

**Method Overview** Figure 1 shows an overview of our approach. We aim to iteratively carve out an interpretable model from the given Blackbox model. Each iteration results in an interpretable model (the downward grey paths in Figure 1) and a residual (the straightforward black paths in Figure 1). We start this process with $f^0$ – the initial Blackbox given to us. At iteration $k$, we distill the Blackbox of the previous iteration $f^{k-1}$ with a neuro-symbolic interpretable model, $g^k : \mathcal{C} \rightarrow \mathcal{Y}$. We generate explanations in terms of First Order Logic (FOL) from $g^k$ as suggested by Barbiero et al. (2022). We coin the term *residual* $r^k$ to refer to the portion of $f^{k-1}$ that $g^k$ cannot explain, specifically $r^k = f^{k-1} - g^k$. We then approximate $r^k$ with $f^k = h^k(\Phi(.))$. $f^k$ will be the Blackbox for the subsequent iterations and be explained by the respective interpretable models. A learnable gating mechanism, denoted by $\pi^k : \mathcal{C} \rightarrow \{0, 1\}$ (shown as the selector in Figure 1) is responsible for routing an input image towards either $g^k$ or $r^k$. The thickness of the lines in Figure 1 represents the samples covered by the interpretable models (grey line) and the residuals (black line). With every iteration, the cumulative coverage of the interpretable models increases, but the residual decreases. We name our method *route, interpret* and *repeat*.

### 3.1 NEURO-SYMBOLIC KNOWLEDGE DISTILLATION

Neuro-symbolic AI is an area of study that encompasses deep neural networks with symbolic approaches to computing and AI to complement the strengths and weaknesses of each, resulting in a robust AI capable of reasoning and cognitive modeling Belle (2020). Neuro-Symbolic knowledge distillation in our method involves three parts. (1) a series of trainable soft attention scores that *routes* each sample through the interpretable models and the residual networks, (2) A sequence of

learnable neuro-symbolic interpretable models, each providing FOL explanations to *interpret* the Blackbox, and (3) *repeating* with Residual networks for the samples that cannot be explained with their interpretable counterparts. We explain each component in detail in what follows.

#### 3.1.1 THE SELECTOR FUNCTION

The first step of our method is to *route* an input sample through the interpretable model $g^k$ and residuals $r^k$ using a series of soft attention scores $\pi^k$ for $k \in [0, K]$, where $K$ is the number of iterations. We denote this as the selector in Figure 1. Specifically, at each iteration $k$, the specific selector *routes* a sample $\{\boldsymbol{x_j}, \boldsymbol{y_j}, \boldsymbol{c_j}\}$ towards $g^k$ and $r^k$ with probability $\pi^k(\boldsymbol{c_j})$ and $1 - \pi^k(\boldsymbol{c_j})$ respectively. We define the empirical coverage of the $k^{th}$ iteration as, $\zeta(\pi^k) = \dfrac{1}{m}\sum_{j=1}^{m} \pi^k(\boldsymbol{c_j})$, the empirical mean of the samples selected by the selector for the corresponding interpretable model $g^k$, with $m$ being the total number of samples in the training set. Thus the total selective risk is,

$$\mathcal{R}^k(\pi^k, g^k) = \frac{\frac{1}{m}\sum_{j=1}^{m} \mathcal{L}^k_{(g^k,\pi^k)}(\boldsymbol{x_j}, \boldsymbol{c_j})}{\zeta(\pi^k)}, \tag{1}$$

where $\mathcal{L}^k_{(g^k,\pi^k)}$ is the optimization loss used to learn $g^k$ and $\pi^k$ together, discussed in section 3.1.2. For a given coverage of $\tau^k \in (0, 1]$, we solve the following optimization problem

$$\theta^*_{s^k}, \theta^*_{g^k} = \min_{\theta_{s^k}, \theta_{g^k}} \mathcal{R}^k\big(\pi^k(.;\theta_{s^k}), g^k(.;\theta_{g^k})\big) \quad \text{s.t.} \quad \zeta\big(\pi^k(.;\theta_{s^k})\big) \geq \tau^k \tag{2}$$

For $k^{th}$ iteration, $\theta^*_{s^k}, \theta^*_{g^k}$ are the optimal parameters for the selector $\pi^k$ and the interpretable model $g^k$ respectively. In this work, $\pi^k$'s are neural networks with sigmoid activation. At inference time, the concept vector $\boldsymbol{c_j}$ of sample $\boldsymbol{x_j}$ is fed to $g^k$ if and only if $\pi^k(\boldsymbol{c}_j) \geq 0.5$ for $k \in [0, K]$.

#### 3.1.2 NEURO-SYMBOLIC INTERPRETABLE MODELS

In this stage for the iteration $k$, we design interpretable model $g^k$ to *interpret* the Blackbox $f^{k-1}$ from the previous iteration $k-1$ by optimizing the following loss function,

$$\mathcal{L}^k_{(g^k,\pi^k)}(\boldsymbol{x_j}, \boldsymbol{c_j}) = \underbrace{\ell\big(f^{k-1}(\boldsymbol{x_j}), g^k(\boldsymbol{c_j})\big)\pi^k(\boldsymbol{c_j})}_{\substack{\text{trainable component}\\ \text{for current iteration } k}} \underbrace{\prod_{i=1}^{k-1}\big(1 - \pi^i(\boldsymbol{c_j})\big)}_{\substack{\text{fixed component trained}\\ \text{in the previous iterations}}} \tag{3}$$

The term multiplied by the loss function $\ell$ in equation 3, is the probability of sample $\boldsymbol{x_j}$ reaching the interpretable model $g^k$, which is the probability of going through the residual for iterations 0 through $k-1$ $\big($i.e. $\prod_{i=1}^{k-1}\big(1 - \pi^i(\boldsymbol{c_j})\big)\big)$ times the probability of going through the interpretable model at iteration $k$ $\big($i.e. $\pi^k(\boldsymbol{c_j})\big)$. Refer to Figure 1 for an illustration. Note that $\pi^1, \ldots \pi^{k-1}$ are learned in the previous iterations and are not trainable at iteration $k$. As each interpretable model $g^k$ specializes in explaining a specific subset of samples (denoted by coverage $\tau$), we refer to it as an *expert* moving forward. We adopted the optimization strategy, discussed in Geifman & El-Yaniv (2019) to optimize equation 2. We discuss the loss function in equation 3 in detail in Appendix A.2. After training, we refer to the interpretable experts of all the iterations as a "Mixture of Interpretable Experts" (MoIE) cumulatively.

#### 3.1.3 THE RESIDUALS

The last step is to *repeat* with the residual $r^k$, as $r^k(\boldsymbol{x_j}, \boldsymbol{c_j}) = f^{k-1}(\boldsymbol{x_j}) - g^k(\boldsymbol{c_j})$, to generate $f^k$, effectively making a new Blackbox for the next iteration $k+1$. Specifically, we train $f^k = h^k\big(\Phi(.)\big)$ to match the residual $r^k$. This step is crucial to make $f^k$ specialize over those samples not covered

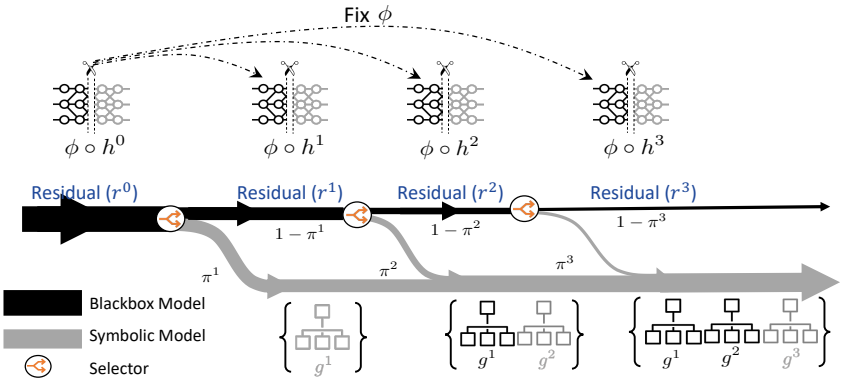


Figure 1: Schematic view of *route, interpret* and *repeat*. At step $k$, the selector *routes* each sample either towards the interpretable model $g^k$ (to *interpret*) with probability $\pi^k$ or the residual (to *repeat* in the further iterations) $r^k = f^{k-1} - g^k$ with probability $1 - \pi^k$. Here, $f^{k-1}$ is the Blackbox of the previous iteration, $k-1$. If the sample goes through $g^k$, we obtain the explanations for that sample in terms of First Order Logic (FOL). Otherwise, the sample goes through the next step until it either goes through a subsequent interpretable model or reaches the last residual. Note that components in black and grey indicate the fixed and trainable modules in our model.

by $g^k$. For the $k^{th}$ iteration, we optimize the following loss function to obtain $f^k$:

$$\mathcal{L}_f^k(\boldsymbol{x_j}, \boldsymbol{c_j}) = \underbrace{\ell\big(r^k(\boldsymbol{x_j}, \boldsymbol{c_j}), f^k(\boldsymbol{x_j})\big)}_{\substack{\text{trainable component} \\ \text{for iteration } k}} \underbrace{\prod_{i=1}^{k} \big(1 - \pi^i(\boldsymbol{c_j})\big)}_{\substack{\text{non-trainable component} \\ \text{for iteration } k}} \tag{4}$$

Notice that the embedding $\Phi(.)$ is fixed for all the iterations. Due to computational reasons, we only update the last few layers of the Blackbox ($h^k$) in order to train $f^k$. At the final iteraion $K$, our method yeilds a MoIE, explaining the interpretable component of the initial Blackbox $f^0$ and the final residual for the uninterpretable component of $f^0$. Algorithm 1 in Appendix A.3 explains the training procedure of our model and extraction of FOL to explain samples locally. Figure 8 in Appendix A.3 shows the architecture of our model at inference.

## 4 Experiments

To validate our method, we utilize four datasets - 1) bird species classification using CUB-200 Wah et al. (2011) dataset, 4) animals species classification using Animals with Attributes2 (Awa2) dataset Xian et al. (2018), 3) skin lesion classification using HAM10000 dataset Tschandl et al. (2018), 4) Effusion and Cardiomegaly classification from radiology images using MIMIC-CXR dataset Johnson et al.. First, we demonstrate that MoIE does not hinder the performance of the Blackbox. Second, we conduct qualitative analysis to illustrate the effectiveness of local explanations. Third, we validate that the cumulative coverage of the residuals decreases over successive iterations. Finally, we leverage the Waterbirds dataset Sagawa et al. (2019) to eliminate shortcut bias in vision datasets.

**Training configurations** As a Blackbox, we use ResNet-101 He et al. (2016) and Vision Transformer (VIT) Wang et al. (2021) for the CUB-200 and Awa2 datasets. For HAM10000 and MIMIC-CXR, we utilize Inception Szegedy et al. (2015) and Densenet-121 Huang et al. (2017) as the same. For CUB-200, we employ six experts each for both VIT and ResNet-based Blackboxes. For Awa2, we utilize 4 and 6 experts for ResNet-101 and VIT, respectively. For HAM10000 and MIMIC-CXR (for both Cardiomegaly and Effusion), we use 5 and 3 experts, respectively. Refer to Appendix A.1 and A.6 for details about the dataset and hyperparameters. Furthermore, we only include concepts as input to $g$ if their validation accuracy or auroc exceeds a certain threshold (in all of our experiments, we fix 0.7 or 70% as the threshold of validation auroc or accuracy). For HAM10000, we use the identical "concept bank" as proposed in Yuksekgonul et al. (2022).

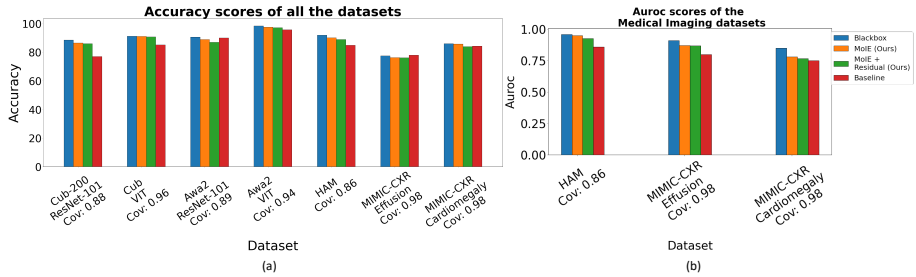


Figure 2: MoIE does not hurt the performance of the Blackbox. From left to right, we compare the (a) accuracy and (b) auroc metrics respectively. For the MoIE (ours), we specify the empirical coverage as *cov* in the figure w.r.t each datasets.

### 4.1 Baseline

Our baseline is based on the *interpretable by design* principle, consisting of two parts: 1) a concept extractor $\phi : \mathcal{X} \rightarrow \mathcal{C}$, a mapping from the image to the concept space; and 2) $g : \mathcal{C} \rightarrow \mathcal{Y}$, a mapping from the concepts to the prediction. We train $\phi$ and $g$ sequentially from scratch with the supervision of the human attributes $\mathcal{C}$ and class labels $\mathcal{Y}$ respectively. The concept extractor $\phi$ for Resnet, Inception, and Densenet121 includes all layers until the last convolution block. The VIT-based $\phi$ consists of the transformer encoder block (excluding the classification head). We use the identical configurations for $g$ as described in Appendix A.6 for each dataset.

### 4.2 Results

#### 4.2.1 Quantitative analysis of MoIE with the blackbox and baseline

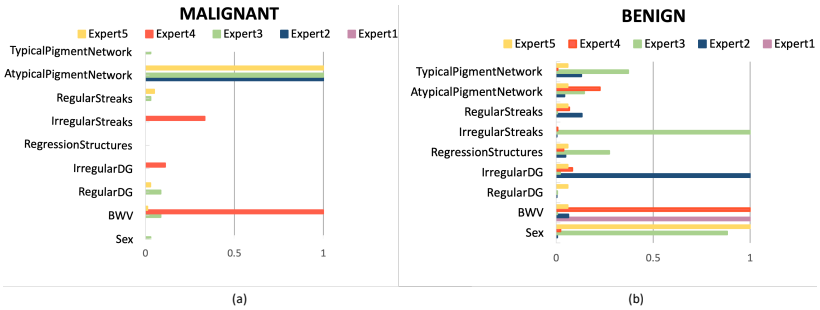


Figure 3: From left to right, for each expert, bar plot showing the importance of a concept for predicting a skin lesion as Malignant and Benign respectively. For example, *atypicalpigmentnetwork* concept plays a crucial role for predicting "Malignant" skin lesion by expert5 as is present in all the local explanations for expert5.

Figure 2 displays the performance of our method using a heldout test set. "MoIE" and "MoIE + Residual" denote the mixture of interpretable experts ($g$) excluding and including the final residual, respectively. Coverage (Cov in the figure) represents the proportion of samples in the test set covered by all the experts throughout iterations. For CUB-200, Awa2, and HAM10000, MoIE achieves similar performance to the Blackbox. For CUB-200 and HAM10000, our method achieves a significant performance gain compared to the baseline. For Awa2, the baseline performs at par with our model. (ResNet-based baseline exceeds ours). Note that all the datasets include noisy concepts except Awa2, making it appropriate for the *interpretable by design* models. In general, VIT-derived experts performed better than their ResNet-based counterparts. The MIMIC-CXR dataset is highly imbalanced, with the positive samples being too few compared to the negative ones. As a result, the baselines for them attain similar accuracy scores as our MoIE model (Figure 2a). Therefore, precision and recall are better metrics for assessing the models' performance on these datasets. To

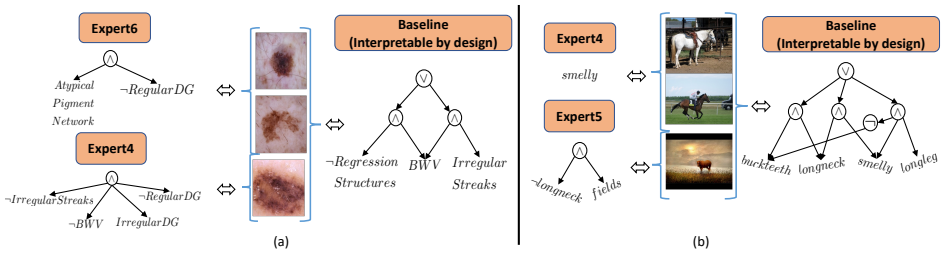


Figure 4: Illustration of flexibility of FOL explanations by MoIE. We report the FOL for different experts and the baseline to identify (a) Malignant lesion and (b) Horse. For example, in Figure (a), the FOL by the baseline composes *BWV*, *RegressionStructures* and *IrregularStreaks* concepts to distinguish all the samples of the skin lesion "Malignant". However in the same Figure (a), expert6 identifies the instances of "Malignant" in the first two rows with *AtypicalPigmentNetwork* and *RegularDG* as the identifying concept. Similarly expert4 classifies the samples of "Malignant" in the third row of Figure (a) using other *BWV*, *IrregularStreaks*, *RegularDG* and *IrregularDG*.

demonstrate this, we plot the auroc in Figure 2b. As it can be seen, MoIE significantly outperforms the baseline in terms of auroc.

### 4.2.2 Local explanations by MoIE

As shown in E-Lens Barbiero et al. (2022), each expert constructs local FOL per sample, composing the concepts based on their attention weights. Due to space constraints, we report the analysis for the FOL explanation of HAM10000 and CUB-200 datasets here; Appendices A.7.8 and A.7.4 include the results of Awa2 and MIMIC-CXR datasets, respectively. Figures 3a-b exhibit a quantitative analysis of the relative frequency of the concepts used by various experts to correctly classify the "Malignant" and "Benign" skin lesions, respectively. As per Figure 3a, local FOLs' of all samples analyzed by experts 2, 3, and 5 include the concept *AtypicalPigmentNetwork*, proving it to be an essential concept for predicting malignancy. Also, expert4 (the red bars in the Figure 3a) classifies "Malignancy," using multiple concepts, such as *IrregularStreaks*, *IrregularDG*, and *Blue Whitish Veil (BWV)*, whereas expert2 (the blue bar in the Figure 3a) just utilizes *AtypicalPigmentNetwork*.

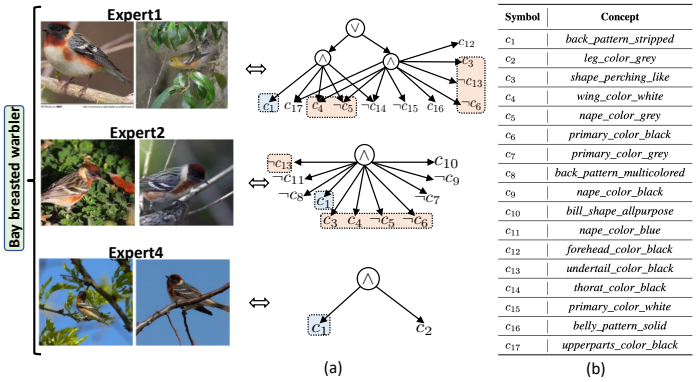


| Symbol | Concept |
|---|---|
| $c_1$ | *back_pattern_stripped* |
| $c_2$ | *leg_color_grey* |
| $c_3$ | *shape_perching_like* |
| $c_4$ | *wing_color_white* |
| $c_5$ | *nape_color_grey* |
| $c_6$ | *primary_color_black* |
| $c_7$ | *primary_color_grey* |
| $c_8$ | *back_pattern_multicolored* |
| $c_9$ | *nape_color_black* |
| $c_{10}$ | *bill_shape_allpurpose* |
| $c_{11}$ | *nape_color_blue* |
| $c_{12}$ | *forehead_color_black* |
| $c_{13}$ | *undertail_color_black* |
| $c_{14}$ | *thorat_color_black* |
| $c_{15}$ | *primary_color_white* |
| $c_{16}$ | *belly_pattern_solid* |
| $c_{17}$ | *upperparts_color_black* |

Figure 5: Illustration of class-level or global explanations. We report the global explanation of "Bay breasted warbler" using the VIT-based blackbox by combining (using DNF) the local explanations. (a) Explanations by expert1 (top row), expert2 (middle row) and expert4 (bottom row). Shared concepts across all the experts are highlighted in blue. We highlight the same for experts 1 and 2 in orange. (b) Symbols used in Figure 3a and their corresponding true concept labels.

Figure 4 compares the FOL explanations by different experts with the baseline. As the baseline includes a single interpretable model $g$, all the FOLs for each sample per class incorporate identical concepts. According to Figure 4a, expert4 relies on *Blue Whitish Veils (BWV)*, *Irregular Streaks*, *Regular* and *Irregular Dots and Globules (DG)* to identify "Malignancy", whereas expert6 utilizes *Rregular Dots and Globules* and *ATypical Pigment Net*. Appendices A.7.8 and A.7.6 display more

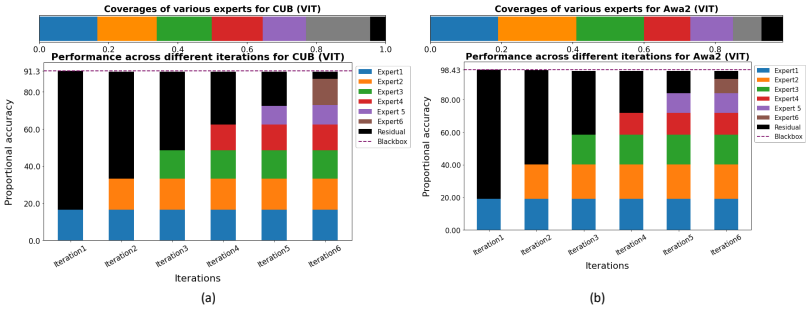


Figure 6: Coverage and performance of each VIT-derived expert and residual for (a) CUB-200 (b) Awa2

qualitative FOLs for Awa2 and HAM10000 datasets respectively. MoIE demonstrates similar flexibility in creating the FOL explanation for Awa2. For example, in 4 b, the baseline utilizes *longneck*, *smelly*, *longleg* and *buckteeth* to identify all the samples of "Horse". MoIE employs the concepts on a per-sample basis, so different experts adopt different concepts to classify the samples of a particular class. In Figure 4 the expert4 uses *smelly*, but the expert5 uses *fields* and *longneck* to distinguish "Horse".

We perform the same analysis for CUB-200 to formulate a global explanation of a class by combining the different local FOLs per sample using *conjunctive normal form* (CNF) as in E-Lens. Figure 5 depicts such global explanations for the species "Bay-breasted warbler" by three distinct experts. Here we capture the heterogeneity in class-level explanations since each FOL corresponding to an expert has an amalgamation of distinct and shared concepts. For instance *leg_color_grey* is unique to expert4, but *belly_pattern_solid* and *back_pattern_multicolored* are unique to experts 1 and 2, respectively.

#### 4.2.3 Performance of each expert and the residual

Figure 6 displays the proportional accuracy of MoIE and the residual for the CUB-200 and Awa2 datasets. Proportional accuracy of each model (experts and/or residuals) is defined as the accuracy of that model times its coverage. Recall that the model's coverage is the empirical mean of the samples selected by the selector. The dashed line in each of the plots indicates the performance of the blackbox, $f^0$, denoting the upper bound of our MoIE models. As shown in Figure 6a, the VIT-derived expert and residual cumulatively achieve an accuracy of approximately 91% for the CUB-200 dataset in iteration 1, where the residual's contribution (black bar) is greater than the expert1's (blue bar). Later iterations reveal that the MoIE's performances cumulatively increase, and the residual worsens. In the final iteration, the MoIE contributes most to performance as they carve out all the interpretable segments from the Blackbox. We observe that the final uninterpretable samples that are routed towards the final residual are "harder" samples for the model to predict, resulting in a lower residual accuracy. Tracing these samples back to $f^0$, we observe that the original blackbox has a similar low performance for predicting these samples. We have shown some of these "hard" images side by side with the ones explained by the experts for CUB-200 in Appendix A.7.7. Also, Table 6 verfies this claim, Per our investigation and as it can be in the images, "hard" examples tend to be blurry or distorted images or ones with birds not fully centered or hard to tell from the background.

As shown in the coverage plot, this experiment reinforces Figure 1, where the flow through the experts gradually becomes thicker compared to the narrower flow of the residual with every iteration. We observe similar trends for the other architectures and datasets. For medical imaging (HAM and MIMIC-CXR) datasets and ResNet-derived experts of vision datasets, refer to figures 12 and 11 in the Appendix A.7.3 and A.7.2, respectively.

### 4.3 Application in removal of shortcuts

To conduct this experiment, we create the Waterbirds dataset as in Sagawa et al. (2019) by spuriously correlating the images of birds from the Caltech-UCSD Birds-200-2011 dataset to the images of

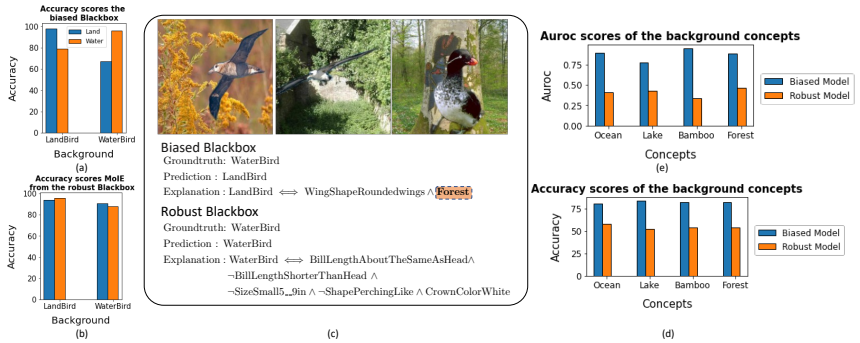


Figure 7: Applying MoIE to eliminate shortcuts. (a) Performance of the biased Blackbox. (b) Performance of final MoIE, trained using the supervision of the robust Blackbox after removing the shortcuts using MDN. (c) Examples of samples and their explanations by the biased (top-row) and robust Blackboxes(bottom-row). (d) auroc and (e) accuracy metrics of the biased Blackbox (when the shortcuts are present) and the robust Blackbox (when the shortcuts are removed using MDN).

land and water background from the Places dataset. Specifically, we use forest and bamboo as the spurious land concepts for landbirds; ocean and lakes as the spurious water concepts for waterbirds. Thus, we have 112 visual concepts (108 concepts from CUB-200 and four new concepts for the background). We aim to identify each bird as a Waterbird or a Landbird. We use ResNet50 (He et al. (2016)) as the Blackbox $f^0$. The Blackbox quickly latches on the spurious background to classify the birds. As a result, the black box's accuracy varies for land-based subsets versus aquatic subsets of the bird species, as shown in Figure 7a. The Waterbird on water is more accurate than on land ((96% vs. 67 % in the orange bar in the Figure 7a). We train $t$ to retrieve the concepts from the biased Blackbox. Next, we train our MoIE to explain the bird species using FOL. As per Figure 7c (middle row), the FOL of a waterbird misclassified as a landbird captures the spurious concept *forest*. Assuming the background concepts as metadata, we aim to reduce the background bias from the representation of the Blackbox using metadata normalization (MDN) Lu et al. (2021). Therefore, we leverage the MDN layers between two successive layers of the convolutional backbone to fine-tune the biased Blackbox. Next, we train $t$, using the embedding $\phi$ of the robust Blackbox. Figures 7d-e compare the auroc and accuracy scores of the spurious background concepts from the embedding $\phi$ of the biased and robust Blackboxes, respectively. The validation auroc (accuracy) of all the spurious concepts retrieved from the robust Blackbox fell well short of the predefined threshold 0.7 (70 %) compared to the biased Blackbox. Finally, we re-train the MoIE distilling from the new robust Blackbox. Figure 7b illustrates that the accuracies of Waterbird on water vs. Waterbird on land become pretty similar (91% -88 %). The FOL from the robust Blackbox does not include any background concepts (Figure 7c, bottom row). Refer to the Figure 9 in Appendix A.5 for the flow diagram of this experiment.

## 5 Discussion & Conclusions

This paper proposes a novel method to iteratively extract a mixture of interpretable models from a trained Blackbox by utilizing the flexibility of the Blackbox to bridge the gap between post hoc explanation and the construction of interpretable models. The comprehensive experiments on a various datasets demonstrate that 1) our model maintains a similar performance compared to the Black box while making it explainable, 2) the local explanations by our model account for the diversity of explanations of the various samples in a dataset, 3) the coverage of the residuals gradually declines over the iterations. Finally, we employ our method to eliminate the shortcuts in images effectively. We identify the concepts from the representation of the blackbox based on correlation, not causation. So, it is still unclear if the blackbox uses those concepts for prediction. A possible future direction can be the discovering only those concepts causally, used by the blackbox for prediction. In the future we also aim to apply our method to other modalities such as text or video.

## REFERENCES


Abubakar Abid, Mert Yuksekgonul, and James Zou. Meaningfully explaining model mistakes using conceptual counterfactuals. *arXiv preprint arXiv:2106.12723*, 2021.

Julius Adebayo, Justin Gilmer, Michael Muelly, Ian Goodfellow, Moritz Hardt, and Been Kim. Sanity checks for saliency maps. *Advances in neural information processing systems*, 31, 2018.

Raed Alharbi, Minh N Vu, and My T Thai. Learning interpretation with explainable knowledge distillation. In *2021 IEEE International Conference on Big Data (Big Data)*, pp. 705–714. IEEE, 2021.

Pietro Barbiero, Gabriele Ciravegna, Francesco Giannini, Pietro Lió, Marco Gori, and Stefano Melacci. Entropy-based logic explanations of neural networks. In *Proceedings of the AAAI Conference on Artificial Intelligence*, volume 36, pp. 6046–6054, 2022.

Vaishak Belle. Symbolic logic meets machine learning: A brief survey in infinite domains. In *International Conference on Scalable Uncertainty Management*, pp. 3–16. Springer, 2020.

L Breiman, J Friedman, CJ Stone, and RA Olshen. Classification and regression trees (crc, boca raton, fl). 1984.

Chaofan Chen, Oscar Li, Daniel Tao, Alina Barnett, Cynthia Rudin, and Jonathan K Su. This looks like that: deep learning for interpretable image recognition. *Advances in neural information processing systems*, 32, 2019.

Xu Cheng, Zhefan Rao, Yilan Chen, and Quanshi Zhang. Explaining knowledge distillation by quantifying the knowledge. In *Proceedings of the IEEE/CVF conference on computer vision and pattern recognition*, pp. 12925–12935, 2020.

Gabriele Ciravegna, Francesco Giannini, Marco Gori, Marco Maggini, and Stefano Melacci. Human-driven fol explanations of deep learning. In *IJCAI*, pp. 2234–2240, 2020a.

Gabriele Ciravegna, Francesco Giannini, Stefano Melacci, Marco Maggini, and Marco Gori. A constraint-based approach to learning and explanation. In *Proceedings of the AAAI Conference on Artificial Intelligence*, volume 34, pp. 3658–3665, 2020b.

Gabriele Ciravegna, Pietro Barbiero, Francesco Giannini, Marco Gori, Pietro Lió, Marco Maggini, and Stefano Melacci. Logic explained networks. *arXiv preprint arXiv:2108.05149*, 2021.

Roxana Daneshjou, Kailas Vodrahalli, Weixin Liang, Roberto A Novoa, Melissa Jenkins, Veronica Rotemberg, Justin Ko, Susan M Swetter, Elizabeth E Bailey, Olivier Gevaert, et al. Disparities in dermatology ai: Assessments using diverse clinical images. *arXiv preprint arXiv:2111.08006*, 2021.

Yonatan Geifman and Ran El-Yaniv. Selectivenet: A deep neural network with an integrated reject option. In *International conference on machine learning*, pp. 2151–2159. PMLR, 2019.

Trevor Hastie and Robert Tibshirani. Generalized additive models: some applications. *Journal of the American Statistical Association*, 82(398):371–386, 1987.

Kaiming He, Xiangyu Zhang, Shaoqing Ren, and Jian Sun. Deep residual learning for image recognition. In *Proceedings of the IEEE conference on computer vision and pattern recognition*, pp. 770–778, 2016.

Geoffrey Hinton, Oriol Vinyals, Jeff Dean, et al. Distilling the knowledge in a neural network. *arXiv preprint arXiv:1503.02531*, 2(7), 2015.

Gao Huang, Zhuang Liu, Laurens Van Der Maaten, and Kilian Q Weinberger. Densely connected convolutional networks. In *Proceedings of the IEEE conference on computer vision and pattern recognition*, pp. 4700–4708, 2017.

Saahil Jain, Ashwin Agrawal, Adriel Saporta, Steven QH Truong, Du Nguyen Duong, Tan Bui, Pierre Chambon, Yuhao Zhang, Matthew P Lungren, Andrew Y Ng, et al. Radgraph: Extracting clinical entities and relations from radiology reports. *arXiv preprint arXiv:2106.14463*, 2021.

Alistair Johnson, Matt Lungren, Yifan Peng, Zhiyong Lu, Roger Mark, Seth Berkowitz, and Steven Horng. Mimic-cxr-jpg-chest radiographs with structured labels.

Jeremy Kawahara, Sara Daneshvar, Giuseppe Argenziano, and Ghassan Hamarneh. Seven-point checklist and skin lesion classification using multitask multimodal neural nets. *IEEE journal of biomedical and health informatics*, 23(2):538–546, 2018.

Been Kim, Martin Wattenberg, Justin Gilmer, Carrie Cai, James Wexler, Fernanda Viegas, and Rory Sayres. Interpretability beyond feature attribution: Quantitative testing with concept activation vectors (tcav).(2017). *arXiv preprint arXiv:1711.11279*, 2017.

Pieter-Jan Kindermans, Sara Hooker, Julius Adebayo, Maximilian Alber, Kristof T Schütt, Sven Dähne, Dumitru Erhan, and Been Kim. The (un) reliability of saliency methods. In *Explainable AI: Interpreting, Explaining and Visualizing Deep Learning*, pp. 267–280. Springer, 2019.

Pang Wei Koh, Thao Nguyen, Yew Siang Tang, Stephen Mussmann, Emma Pierson, Been Kim, and Percy Liang. Concept bottleneck models. In *International Conference on Machine Learning*, pp. 5338–5348. PMLR, 2020.

Benjamin Letham, Cynthia Rudin, Tyler H McCormick, and David Madigan. Interpretable classifiers using rules and bayesian analysis: Building a better stroke prediction model. *The Annals of Applied Statistics*, 9(3):1350–1371, 2015.

Mandy Lu, Qingyu Zhao, Jiequan Zhang, Kilian M Pohl, Li Fei-Fei, Juan Carlos Niebles, and Ehsan Adeli. Metadata normalization. In *Proceedings of the IEEE/CVF Conference on Computer Vision and Pattern Recognition*, pp. 10917–10927, 2021.

Adriano Lucieri, Muhammad Naseer Bajwa, Stephan Alexander Braun, Muhammad Imran Malik, Andreas Dengel, and Sheraz Ahmed. On interpretability of deep learning based skin lesion classifiers using concept activation vectors. In *2020 international joint conference on neural networks (IJCNN)*, pp. 1–10. IEEE, 2020.

Scott M Lundberg and Su-In Lee. A unified approach to interpreting model predictions. In *Proceedings of the 31st international conference on neural information processing systems*, pp. 4768–4777, 2017.

Grégoire Montavon, Wojciech Samek, and Klaus-Robert Müller. Methods for interpreting and understanding deep neural networks. *Digital signal processing*, 73:1–15, 2018.

Meike Nauta, Ron van Bree, and Christin Seifert. Neural prototype trees for interpretable fine-grained image recognition. In *Proceedings of the IEEE/CVF Conference on Computer Vision and Pattern Recognition*, pp. 14933–14943, 2021.

Marco Tulio Ribeiro, Sameer Singh, and Carlos Guestrin. " why should i trust you?" explaining the predictions of any classifier. In *Proceedings of the 22nd ACM SIGKDD international conference on knowledge discovery and data mining*, pp. 1135–1144, 2016.

Cynthia Rudin. Stop explaining black box machine learning models for high stakes decisions and use interpretable models instead. *Nature Machine Intelligence*, 1(5):206–215, 2019.

Shiori Sagawa, Pang Wei Koh, Tatsunori B Hashimoto, and Percy Liang. Distributionally robust neural networks for group shifts: On the importance of regularization for worst-case generalization. *arXiv preprint arXiv:1911.08731*, 2019.

Wojciech Samek, Alexander Binder, Grégoire Montavon, Sebastian Lapuschkin, and Klaus-Robert Müller. Evaluating the visualization of what a deep neural network has learned. *IEEE transactions on neural networks and learning systems*, 28(11):2660–2673, 2016.

Ramprasaath R Selvaraju, Michael Cogswell, Abhishek Das, Ramakrishna Vedantam, Devi Parikh, and Dhruv Batra. Grad-cam: Visual explanations from deep networks via gradient-based localization. In *Proceedings of the IEEE international conference on computer vision*, pp. 618–626, 2017.

Avanti Shrikumar, Peyton Greenside, Anna Shcherbina, and Anshul Kundaje. Not just a black box: Learning important features through propagating activation differences. *arXiv preprint arXiv:1605.01713*, 2016.

Karen Simonyan, Andrea Vedaldi, and Andrew Zisserman. Deep inside convolutional networks: Visualising image classification models and saliency maps. *arXiv preprint arXiv:1312.6034*, 2013.

Sumedha Singla, Brian Pollack, Junxiang Chen, and Kayhan Batmanghelich. Explanation by progressive exaggeration. *arXiv preprint arXiv:1911.00483*, 2019.

Daniel Smilkov, Nikhil Thorat, Been Kim, Fernanda Viégas, and Martin Wattenberg. Smoothgrad: removing noise by adding noise. *arXiv preprint arXiv:1706.03825*, 2017.

Christian Szegedy, Wei Liu, Yangqing Jia, Pierre Sermanet, Scott Reed, Dragomir Anguelov, Dumitru Erhan, Vincent Vanhoucke, and Andrew Rabinovich. Going deeper with convolutions. In *Proceedings of the IEEE conference on computer vision and pattern recognition*, pp. 1–9, 2015.

Philipp Tschandl, Cliff Rosendahl, and Harald Kittler. The ham10000 dataset, a large collection of multi-source dermatoscopic images of common pigmented skin lesions. *Scientific data*, 5(1):1–9, 2018.

David Wadden, Ulme Wennberg, Yi Luan, and Hannaneh Hajishirzi. Entity, relation, and event extraction with contextualized span representations. In *Proceedings of the 2019 Conference on Empirical Methods in Natural Language Processing and the 9th International Joint Conference on Natural Language Processing (EMNLP-IJCNLP)*, pp. 5784–5789, Hong Kong, China, November 2019. Association for Computational Linguistics. doi: 10.18653/v1/D19-1585. URL https://aclanthology.org/D19-1585.

Catherine Wah, Steve Branson, Peter Welinder, Pietro Perona, and Serge Belongie. The caltech-ucsd birds-200-2011 dataset. 2011.

Charles Wan, Rodrigo Belo, and Leid Zejnilovic. Explainability's gain is optimality's loss? how explanations bias decision-making. In *Proceedings of the 2022 AAAI/ACM Conference on AI, Ethics, and Society*, pp. 778–787, 2022.

Jun Wang, Xiaohan Yu, and Yongsheng Gao. Feature fusion vision transformer for fine-grained visual categorization. *arXiv preprint arXiv:2107.02341*, 2021.

Yongqin Xian, Christoph H Lampert, Bernt Schiele, and Zeynep Akata. Zero-shot learning—a comprehensive evaluation of the good, the bad and the ugly. *IEEE transactions on pattern analysis and machine intelligence*, 41(9):2251–2265, 2018.

Ke Yu, Shantanu Ghosh, Zhexiong Liu, Christopher Deible, and Kayhan Batmanghelich. Anatomy-guided weakly-supervised abnormality localization in chest x-rays. *arXiv preprint arXiv:2206.12704*, 2022.

Mert Yuksekgonul, Maggie Wang, and James Zou. Post-hoc concept bottleneck models. *arXiv preprint arXiv:2205.15480*, 2022.